nature communications

Article

https://doi.org/10.1038/s41467-026-70470-8

A blueprint for local and distal invasion programs in glioblastoma

Received: 1 November 2024

Accepted: 22 February 2026

Rony Chanoch-Myers[1,2,3,16], Toshiro Hara[3,4,5,6,16,17] ✉, Alissa C. Greenwald[1,7,8,16], Rouven Hoefflin[1,9], Lillian Bussema[3,4], Hannah R. Weisman[3,4], Edwin Nieblas-Bedolla[5,6], Jahnavi Gurramkonda[5,6], Zhibek Bekezhankyzy[5,6], Alexander Jucht[3,4], Ester Calvo Fernández[3,4], Avishay Spitzer[1,10,11], Jeremy Man Hon Fung[4], Biella Chiara[12], Wajd N. Al-Holou[5], Sandra Camelo-Piragua[13], Jinan Behnan[14], Rossella Galli[12], Hiroaki Wakimoto[15], Mario L. Suvà[3,4,17] ✉ & Itay Tirosh[1,17] ✉

Glioblastoma invasion into brain parenchyma presents significant challenges for treatment but remains poorly understood. In this study, we combine single-cell RNA sequencing, spatial transcriptomics, and multiplexed imaging of orthotopic xenograft models to investigate glioblastoma invasion. We first screen 20 patient-derived gliomasphere models for their distal (i.e., extending to the contralateral hemisphere) and local invasive potential in mice. We show that models with distal invasion potential are enriched with oligodendrocyte progenitor-like cells, while models with only local invasion potential are enriched with mesenchymal-like cells. These patterns reflect predominantly peri-axonal *vs* peri-vascular invasion routes, respectively. Next, we analyze the transcriptomes of invading cells within models (compared to tumor core) and identify programs associated with distal and local invasion. Thus, we decouple transcriptional features associated with invasion potential from those associated with the process of invasion. We validate our findings by spatial transcriptomics and multiplexed imaging, further describing the spatial niche of invasive cells. Taken together, our results provide a blueprint for the invasive potential of glioblastoma cell states and of the programs associated with invasion across different scales.

Glioblastoma, isocitrate dehydrogenase (IDH)-wildtype (hereafter GBM), is an incurable primary brain tumor that inevitably recurs despite maximal surgery and adjuvant chemoradiotherapy[1–4]. A major obstacle to treatment is the topographically diffuse nature of GBM cells[5,6]. Gross total resection of tumors (defined as resection without detectable residual tumor by imaging) extends recurrence-free survival[7,8]; however, clinically undetectable GBM cells that spread beyond the tumor cavity invariably lead to tumor recurrence. Importantly, invasion of the brain parenchyma by GBM cells occurs both locally and distally, with the inter-hemispheric white matter tracts (e.g., corpus callosum) allowing GBM to extend their reach to the contralateral hemisphere[9,10]. Landmark histopathology and molecular studies highlighted that invasion of the brain parenchyma by malignant cells tends to occur along preexisting brain anatomical structures, primarily white matter tracts (peri-axonal) and blood vessels (peri-vascular), which constitute the so-called Scherer secondary structures[9,11–14].

Dissecting the molecular features of invading GBM cells is of critical importance and may contribute to identifying therapeutic opportunities to limit GBM recurrence. Single-cell RNA-sequencing (scRNA-seq) analyses of GBM have identified malignant cell states recapitulating distorted versions of normal neurodevelopment cell types, including oligodendrocyte progenitor (OPC)-like, neural

---

A full list of affiliations appears at the end of the paper. ✉e-mail: hara@umich.edu; Suva.Mario@mgh.harvard.edu; Itay.tirosh@weizmann.ac.il

progenitor (NPC)-like, and astrocyte (AC)-like states, as well as the mesenchymal (MES)-like state, which is regulated by the tumor microenvironment (TME)[15–19]. MES-like programs in GBM have been suggested to underlie GBM invasion, given their similarity to the epithelial-to-mesenchymal transition (EMT) programs associated with invasion and metastasis in epithelial cancers[20,21]. Consistently, in vitro studies have indicated that MES-like GBM cells may exhibit migratory and invasive phenotypes[22–25]. In contrast, other studies suggest the enrichment of progenitor-like transcriptional states at the periphery of GBM[26,27] and of MES-like programs at the tumor core[18,28]. A recent study leveraging PDX models coupled with a gap junction-permeable dye and in vivo microscopy proposed that GBM invasion is primarily driven by “unconnected” GBM cells that are enriched for neurodevelopmental progenitor states (OPC/NPC-like)[29]. Thus, it is plausible that more than one GBM state may be responsible for invasion, and that each invasion-associated state may have differing interactions with non-malignant cell types and unique TME associations.

Prior studies aiming to profile invasive cells by scRNA-seq were limited to cells from the adjacent infiltrating edge or “rim” of bulk tumors[30,31]. We hypothesized that distance from primary site and route of invasion may influence the invasion phenotype. Accordingly, we sought to analyze both local (ipsilateral) and distal (contralateral) invasive GBM cells and to separately analyze peri-vascular invasion and peri-axonal/neuronal invasion. To establish a controllable system for these variables, we relied on GBM xenografts that recapitulate various patterns of GBM invasion[29,32,33].

In this work, we directly profiled invasive GBM cells and their matched tumor core cells in mouse intracranial xenografts by scRNA-seq. We first identified expression differences *between* distally invasive and locally invasive GBM models, uncovering associations of cellular states with the *propensity* for distinct infiltration patterns. We then analyzed the states of invading cells *within* invasive models and uncovered transcriptional programs associated with route-specific invasion. We validated our findings by spatial transcriptomics and antibody-based multiplexed imaging, and additionally explored the TME associations of invasive cells. Taken together, we delineate the invasive potential and the programs associated with GBM invasion through diverse anatomical routes.

Results

A pooled in vivo PDX system reveals differential capacity for distal invasion in GBM models

We first aimed to investigate the capacity of GBM cells for distal invasion in patient-derived xenograft (PDX) models. Previous work showed that only about 20% of GBM PDX models invade the contralateral hemisphere[32]. We therefore sought to test the distal invasive capacity of different GBM patient-derived gliomasphere models and compare the expression profiles of distally invasive and non-distally invasive models.

We developed a pooled in vivo system to simultaneously analyze the distal invasion capacity of multiple patient-derived GBM models. In this assay, we grew 20 GBM patient-derived gliomasphere models separately and pooled them for stereotaxic injection into the brains of mice (10 models per pool−[Pool #1, Pool #2], each with 2 mice replicates) (Fig. 1a). At symptom onset, the mice were euthanized, and brains were dissected under a stereomicroscope and separated into the primary injection site and the contralateral hemispheric invasion fractions (Fig. 1b, c). Malignant cells from each site were isolated by flow cytometry based on GFP expression and profiled by scRNA-seq using the 10X Genomics 3’ gene expression platform (Figure. S1a, b). Since each GBM model has a unique genetic and expression profile, the identity of each cell could be robustly assigned to one model. For assigning model identity within each pool, we utilized a combined approach, including calling SNPs[34,35] and comparing overall transcriptomes to those of gliomasphere models profiled in vitro, as previously described[36] (Figure. S1c–e, **Methods**). In each pool, a single model made up the majority (~70%) of detected malignant cells within the resulting tumor core, while about half of the models were not detected, suggesting a competition between models in their expansion capabilities (Fig. 1d). Distally invasive cells, defined as those found in the contralateral hemisphere, were primarily derived from three highly invasive GBM models (L0627, L0104, GS143), with 53-83% of cells from each of these models detected in the contralateral hemisphere (Fig. 1e). A fourth GBM model (MGG75) was moderately invasive, with 11% of its cells in the contralateral hemisphere, while the remaining models had minimal to no distally invasive cells (Fig. 1e and Figure. S1f).

To validate our results and avoid the confounding effects of our multiplexing strategy, we generated stereotactic xenografts of each of the individual four distally invasive models described above, as well as two noninvasive models (MGG72, MGG65), and MGG123, a model with local ipsilateral invasion[37]. Consistent with the pooled results, we observed distal invasion in L0627, L0104, GS143, and to a lesser extent in MGG75, while no malignant cells were detected in the contralateral hemisphere in the other models (Fig. 1f and Figure S1f, g). Histological analysis confirmed tumor cell infiltration into the brain parenchyma in each of the three top distal-invasion models (Fig. 1g). L0104 appeared to have the most robust invasion phenotype (>80% of invasive tumor cells, Fig. 1e, f), and developed peri-neuronal satellitosis, as observed in human GBM[38] (Fig. 1g).

Between-models analysis: Distal invasion potential is correlated with an OPC-like transcriptional program

To identify expression features of distal invasion models, we integrated our dataset with a previously published compendium of 29 GBM PDXs assessed for their invasiveness across the hemispheres (by a score of I-IV) and profiled by bulk RNAseq[32]. Distally invasive models consistently upregulated 204 genes (Supplementary Data 1), which were significantly enriched (FDR < 0.05) for the OPC-like (*e.g., OLIG2, TNR*) and NPC1-like metaprograms (*e.g., SOX11, DLL1*) (Fig. 2A and Figure S2A). Distally invasive models also consistently downregulated 171 genes (Supplementary Data 1), which were enriched for MES-related genes (e.g., *TIMP1, ANXA2*, and *EMP1)* (Fig. 2A and Figure S2A).

When examining the distribution of previously defined GBM cellular states in our models, we found that the tumor cores of distally invasive models were depleted of MES-like cells and enriched with OPC-like, NPC-like and AC-like cells compared to the non-invasive models (Figure. S2b). However, only the OPC-like enrichment was statistically significant (Figure. S2b, $p = 0.033$, Wilcoxon rank test). Notably, out of the ten models with sufficient data, OPC-like cells were robustly present (>5% of cells) in the tumor cores of five models and were largely absent (<1% of cells) in the remaining five models, and this dichotomy was consistent with the invasive capacity of the models, with only one exception (Fig. 1e). We thus conclude that the capacity for distal invasion is linked primarily to abundance of the OPC-like state, perhaps relating to the extensive migratory capability of normal OPCs across the developing brain[39] and that distal invasion capacity is, in fact, negatively associated with MES-like and AC-like states.

Our observed pattern is consistent with the knowledge that distal invasion primarily occurs by crossing inter-hemispheric white matter tracts such as the corpus callosum, thus primarily reflecting peri-axonal invasion. In line with this, antibody-based multiplexed imaging (CODEX) of a distally invasive model (L0627) demonstrated that SOX2 + OLIG2+ malignant cells invade along white matter tracts (MOG +), consistent with peri-axonal invasion (Fig. 2b).

While distal invasion proceeds along axonal tracts and is associated with OPC-like states, cancer cells can also infiltrate the brain via alternative routes. We hypothesized that some of the tumor-forming models that did not have detectable distal invasion may still show local invasion along other routes, such as along blood vessels[9]. Accordingly, we found direct evidence of peri-vascular invasion in two models (MGG65 and MGG123) within the ipsilateral hemisphere[37] (Fig. 2c, d and Figure S2c–e).

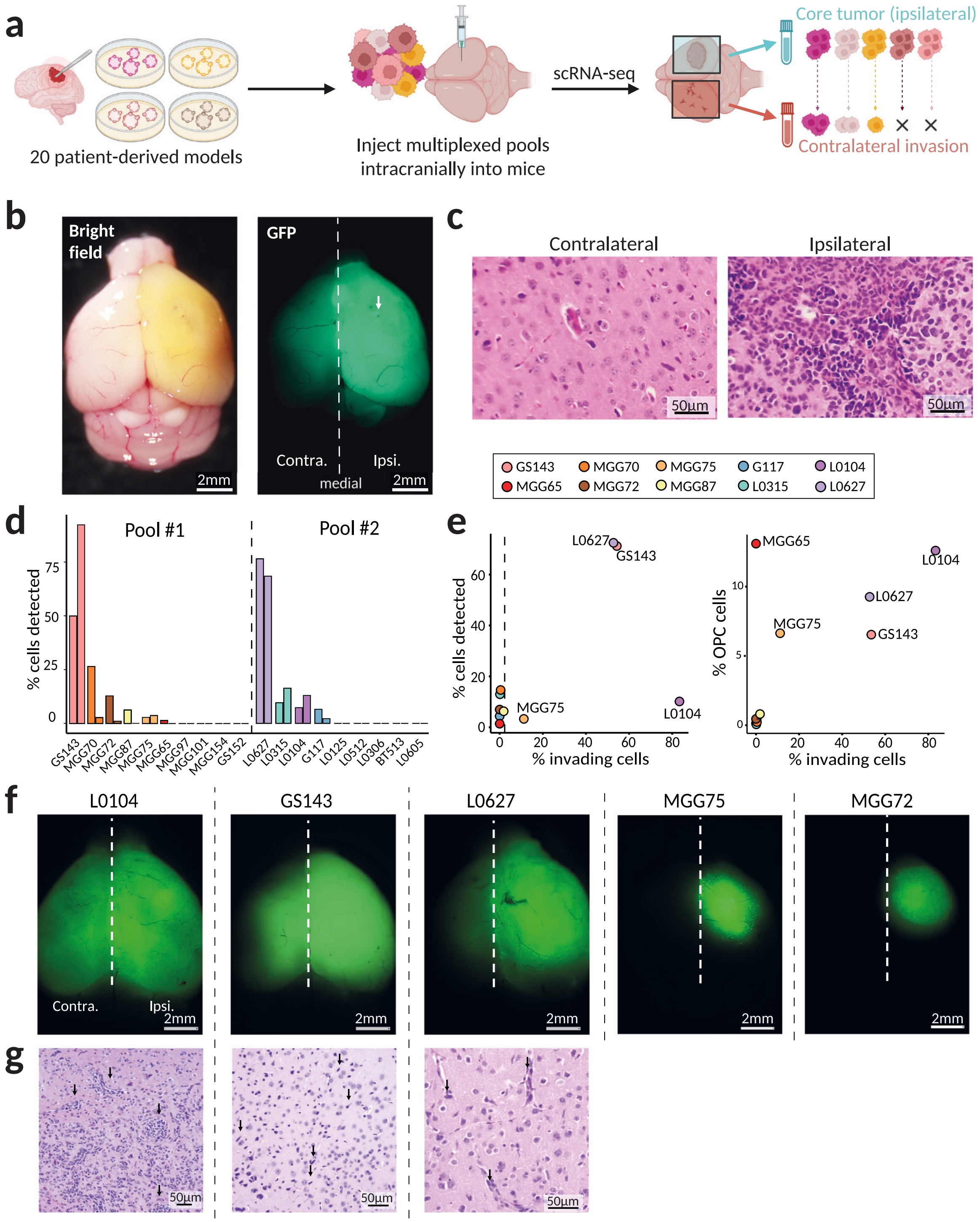

Fig. 1 | In vivo multiplex PDX system to compare tumor formation and invasion capabilities between GBM patient-derived models. a Experimental schematic for multiplexed profiling system. Twenty patient-derived GBM models were multiplexed (10 models per pool, 2 pools) and injected into mice (2 replicates per pool). After tumors formed and invasion occurred, hemispheres were separately dissociated and profiled by singe-cell RNA-seq. Created in BioRender. Chanoch-Myers R. et al. (https://BioRender.com/tapgj56) **b** Brightfield (left) and GFP fluorescence (right) images of whole brain, representative of four mice profiled, from mouse orthotopically injected with GFP-labeled, multiplexed GBM cells (white arrow; injection site). **c** Representative hematoxylin and eosin (H&E) stained brain tissue slides, among two mouse samples analyzed, from ipsilateral and contralateral hemispheres, showing distinct chromatin density pattern between the hemispheres. **d** Barplot shows the percent of each multiplex pool tumor that belonged to each model of origin. Bars are colored by model, each model has two replicates which are shown next to each other. **e** Scatterplots show the average percent of the tumor that belonged to each model (X axis) against either the percent of the cells detected from that model at the contralateral invasive site (Y axis, left panel), or the average percent of the tumor that expressed the OPC-like state (Y axis, right panel). **f** Representative GFP fluorescence images of whole brain from mice orthotopically injected with the model indicated at the top. Models are ordered by the amount of invasion that was detected by the multiplex experiment. **g** Representative H&E stained brain tissue slides, among two mouse samples analyzed, of invasive cells at the contralateral hemisphere for each model. Black arrow indicates pathological findings of glioma satellitosis. Source data are provided as a Source Data file.

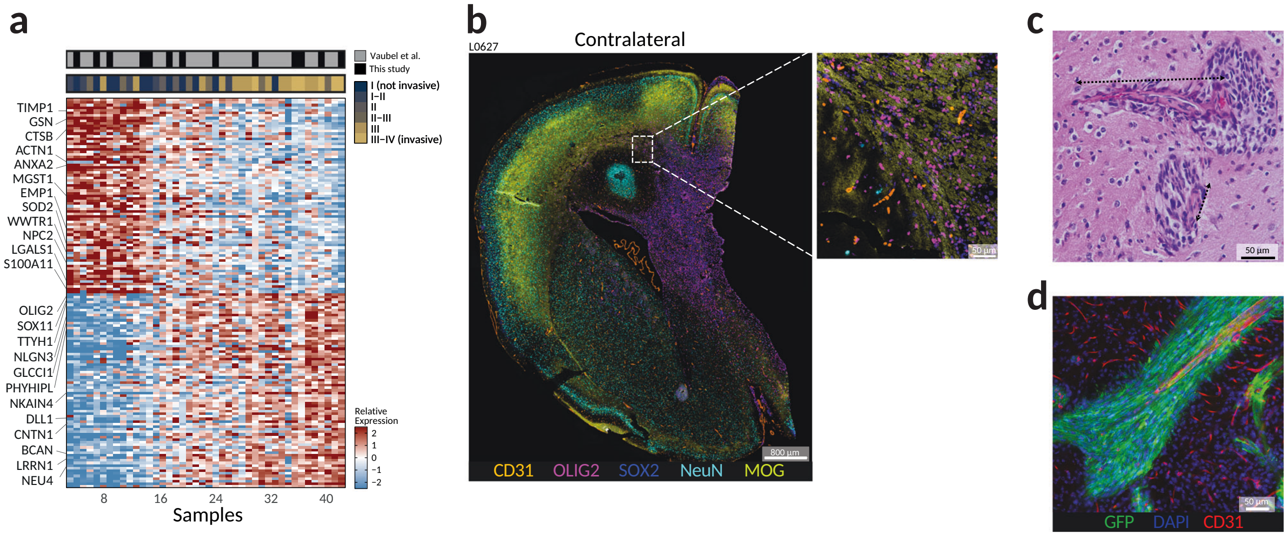

Fig. 2 | The OPC-like state is associated with contralateral invasion of GBM. **a** Heatmap shows the pseudobulk average expression of the tumor core cells from each model from the multiplex experiment, combined with bulk RNA-seq of GBM PDXs from Vaubel et al. The samples are ordered by their expression of the differentially expressed genes between invasive and non-invasive models. The annotation bars show the origin of the data (top) and the Invasion Score for each sample (middle). The Invasion Score was taken from Vaubel et al., and for samples from this study, invasive samples received a score of IV and non-invasive samples received a score of I. **b** Representative CODEX image among three models profiled showing peri-axonal infiltration of the contralateral hemisphere by OPC glioma cells (SOX2 + OLIG2 +) along the white matter tracts (MOG +). **c** Representative H&E stained brain tissue with MGG123 models among two mouse samples analyzed, showing peri-vascular abnormality with cells with highly dense chromatin structures. Arrowed dashed line highlights the vascular endothelium surrounded by malignant cells. **d** Representative confocal imaging of GFP+ tumor cells invading along blood vessels (CD31 +), among two mouse samples analyzed.

Within-models analysis: a consensus transcriptional program defines distally invading cells

While inter-model comparisons revealed features associated with the capacity for distal invasion, we next sought to identify transcriptional programs specifically enriched in cells undergoing invasion. For this, we leveraged the paired single-cell RNA-seq profiles of malignant cells from both the tumor core and the contralateral hemisphere within each model. This allowed us to identify a set of genes upregulated or downregulated in distally invasive cells, (i.e., found in the contralateral hemisphere). By comparing such genes across models, we then identified a set of consensus genes that were consistently upregulated or downregulated in distally-invading glioma (DiG) across models (Fig. 3A, Supplementary Data 2).

The DiG downregulated signature was significantly enriched (FDR < 0.05) with AC-like and MES-like genes (Fig. 3a and Figure S3a). In contrast, the DiG upregulated signature was significantly enriched with NPC-like (*e.g., DLL3, DCX*), OPC-like (*e.g., OLIG1, CADM2)* and cell cycle (*e.g., MKI67*) genes, and included invasion-related regulators not found in the core GBM cell states, such as *ZEB1*—a transcription factor recently implicated in GBM infiltration[40] (Fig. 3a and Figure S3a). Mapping individual cells to the DiG invasion signature revealed that this signature highlights a subset of cells with limited similarity to the OPC-like and NPC-like states and to other signatures involved in GBM invasion[29] (Fig. 3b and Figure S3b, c). Thus, the DiG program represents a distinct transcriptional state induced during distal invasion, rather than a simple subset of pre-existing lineages.

The enrichment of cell cycle genes in the DiG upregulated signature prompted us to examine the distribution of cycling cells across samples. In all three distal invasion models, cycling genes were significantly enriched in cells that upregulated the DiG signature (Figure. S3D; $p < 0.005$, hypergeometric test), consistent with recent studies that highlighted the proliferation of invasive and progenitor-like GBM cells[41]. This result was observed within NPC/OPC-like cells and within AC/MES-like cells, again highlighting that the DiG signature is distinct from the previously defined Neftel states[16] (Figure. S3E).

To investigate the dynamics and spatial distribution of the DiG program during the invasion process, we turned to spatial transcriptomics using the 10x Visium platform. We profiled both hemispheres of GS143 (by both Visium and Visium HD) and integrated our data with an external Visium dataset[42] including three additional distally invasive models (n = 5 mice total; Supplementary Data 3). In PDX models, malignant cells are of human origin, while non-malignant TME cells are of mouse origin, enabling us to confidently distinguish malignant reads from TME reads such that spots could be annotated as TME-dominated, cancer-dominated, or mixed (Fig. 3c).

To examine the spatial distribution of the DiG program across locations during the distal invasion process, we segregated PDX samples of whole brain into four regions: tumor core, tumor periphery, medial, and contralateral (Fig. 3d, Methods). Across all models, the DiG program and cell cycle were increasingly upregulated by malignant cells as they are distancing from the tumor core (Fig. 3d and Figure S3f–h, $p < 0.008$ for each model, Wilcoxon rank test), suggesting an active invasion state rather than a program expressed at the culmination of invasion. In parallel, DiG downregulated genes gradually decreased in expression along this spatial axis. To further examine its temporal dynamics, we analyzed an external Visium PDX gliomasphere dataset in which the same model was profiled at different stages of the invasion process (Fig. 3d). We found that the DiG program was highly expressed in the medial region and contralateral hemisphere during the early stages of invasion. In contrast, at a later stage, the expression of DiG was subsequently lower within the medial region and mostly confined to the contralateral hemisphere, suggesting that cells that have already undergone invasion begin to downregulate the DiG program.

Trajectory inference of single-cell transcriptomes revealed a pseudo-temporal progression from tumor core cells through a DiG-high state and into a cycling DiG state, consistent with a model in which cells first upregulate DiG and later also upregulate cell cycle genes (Figure. S3i–k). Accordingly, ST analysis identified a spatial DiG and periphery DiG program, the latter reflecting malignant cells that invaded furthest, reaching the cortical layers of the brain (Figure. S3l,

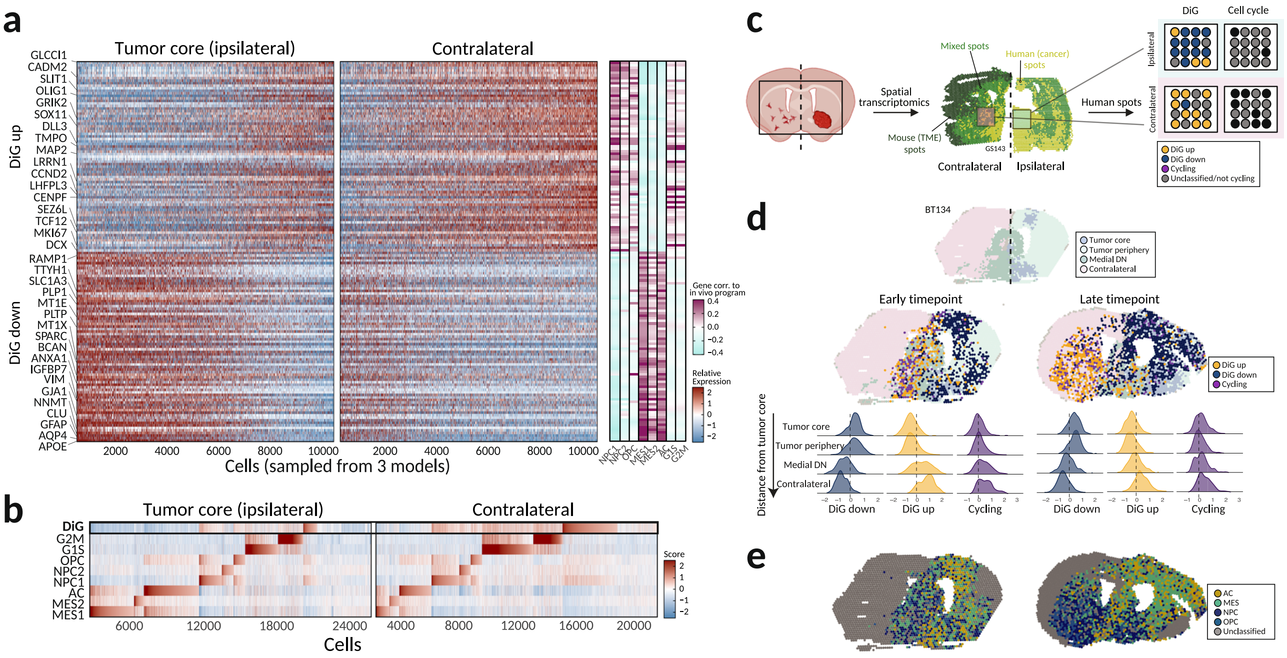

Fig. 3 | Profiling distally invading cells. a Main heatmaps show the expression of spatial DiG program genes (bottom: downregulated, top:upregulated) in the tumor core cells (left) and contralaterally invasive cells (middle). Heatmap on the right shows the correlation of each gene to the average expression of each of the GBM metaprograms from Neftel et al. **b** Heatmaps show scores for the GBM metaprograms from Neftel et al. and spatial DiG (top) for cells from the tumor core (left) or contralateral invasive cells (left). **c** Experimental schematic for spatial validation. Both hemispheres of invasive PDX samples are profiled by Visium spatial transcriptomics. Spots are assigned by species origin as cancer or TME, as well as mixed. Spots containing human cells are scored for spatial DiG program and cell cycle to validate previous findings. Created in BioRender. Chanoch-Myers R. et al. (https://BioRender.com/eglf8l5) (**d**) Top: Spatial map of sample BT134[42], segregated into 4 regions: tumor core, periphery tumor, medial, and contralateral. Bottom and middle: Spatial maps and distribution of scores for the programs, left to right: DiG down, DiG up, and cell cycle genes at each of the 4 regions for an early timepoint (213 days, left) or late timepoint (332 days, right). **e** Spatial maps from (**d**) colored by Neftel cell states.

and Supplementary Data 4). The periphery DiG cells were highly proliferative (17% cycling, compared to 4.8% cycling for DiG), consistent with the neuronal microenvironment promoting the proliferation of glioma cells (Figure. S3l)[43].

We next asked how the Neftel cell states[16] are spatially distributed within the tumor core and across the contralateral hemisphere. We found that the NPC-like and OPC-like states were consistently enriched in the contralateral hemisphere in three out of four models, while the AC-like state was consistently depleted in the contralateral hemisphere of all models ($p = 0.002$) (Fig. 3e and Figure S3m, n). In the GS143 model in particular, the interhemispheric white matter marked an abrupt transition point for AC-like depletion (Figure. S3n), suggesting that the physical constraints and/or cell type composition of white matter tracts may result in a rapid state transition, consistent with the notion that OPC/NPC-like cells are the states endowed with peri-axonal invasion potential[44].

A signature of local peri-vascular invasion in MES-like tumors

As noted above, models lacking distal spread may instead invade locally along blood vessels, possibly upregulating a distinct transcriptional state. To characterize the programs expressed by locally-invading glioma (LiG), we employed fluorescent-guided microdissection and isolated around 200 malignant cells associated with vasculature within the ipsilateral hemisphere of two non-distally invasive models (MGG65 and MGG123) (Fig. 2c, d and Figure S2c–e). These cells were profiled by scRNA-seq, along with around 200 cells of the tumor core of each model. As described for the DiG program, we defined signatures consisting of genes recurrently upregulated and downregulated in LiG compared to cells from their matched tumor cores (Fig. 4a and Figure S4a, b, Supplementary Data 2).

The LiG up-regulated program was enriched (FDR < 0.05) with AC-like genes (e.g., *CLU*) and OPC-like genes (e.g., *ALCAM, NLGN3*) (Figure. S4b, c). However, as observed with DiG, the LiG up-regulated program was distinct from the previously defined states and was specifically enriched in the context of peri-vascular invasion (Fig. 4b). Additionally, cells from the tumor core in LiG models up-regulated mesenchymal genes, including ECM genes (e.g., *FN1, COL11A1, LAMB1*) and ECM-remodeling enzymes (*MMP2, LOXL2*). Multiplexed imaging confirmed the presence of cancer cells exhibiting local invasion along blood vessels (CD31) upregulating AC-OPC markers (i.e., EGFR, OLIG2) as well as ECM-remodeling (glyco-)proteins (e.g., tenascin-C, TNC) (Fig. 4c, d), suggesting that LiG may rely on ECM interactions for peri-vascular invasion. Furthermore, ST analysis revealed a local blood vessel invasion signature (spatial-LiG) that was localized to vascular spots of the ipsilateral hemisphere at the periphery of the tumor core (Fig. 4E, Supplementary Data 4) and correlated with the single-cell LiG program ($r = 0.43$, $p < 2.2 \times 10 - 16$ for MGG123, $r = 0.32$, $p = 7.8 \times 10 - 12$ for MGG65) (Figure. S4D). Similar to the LiG program, the spatial LiG was significantly enriched for AC-like genes (Supplementary Data 4).

Distinct cell states reflect the propensity for invasion vs. the process of invasion

While GBM invasion is often described as a single phenotype, our analyses show multiple associations of cellular states (i.e., expression signatures) with invasion-related phenotypes, highlighting two important distinctions. First, different routes of invasion may rely on distinct mechanisms and hence are associated with different cellular states. Indeed, while peri-axonal invasion is positively associated with OPC-like cells and negatively associated with MES-like cells, the inverse associations to those states are observed in peri-vascular invasion.

Second, even within a single route of invasion, the basal states associated with the propensity for a specific invasion route may not be the same as the states that are observed during the process of invasion,

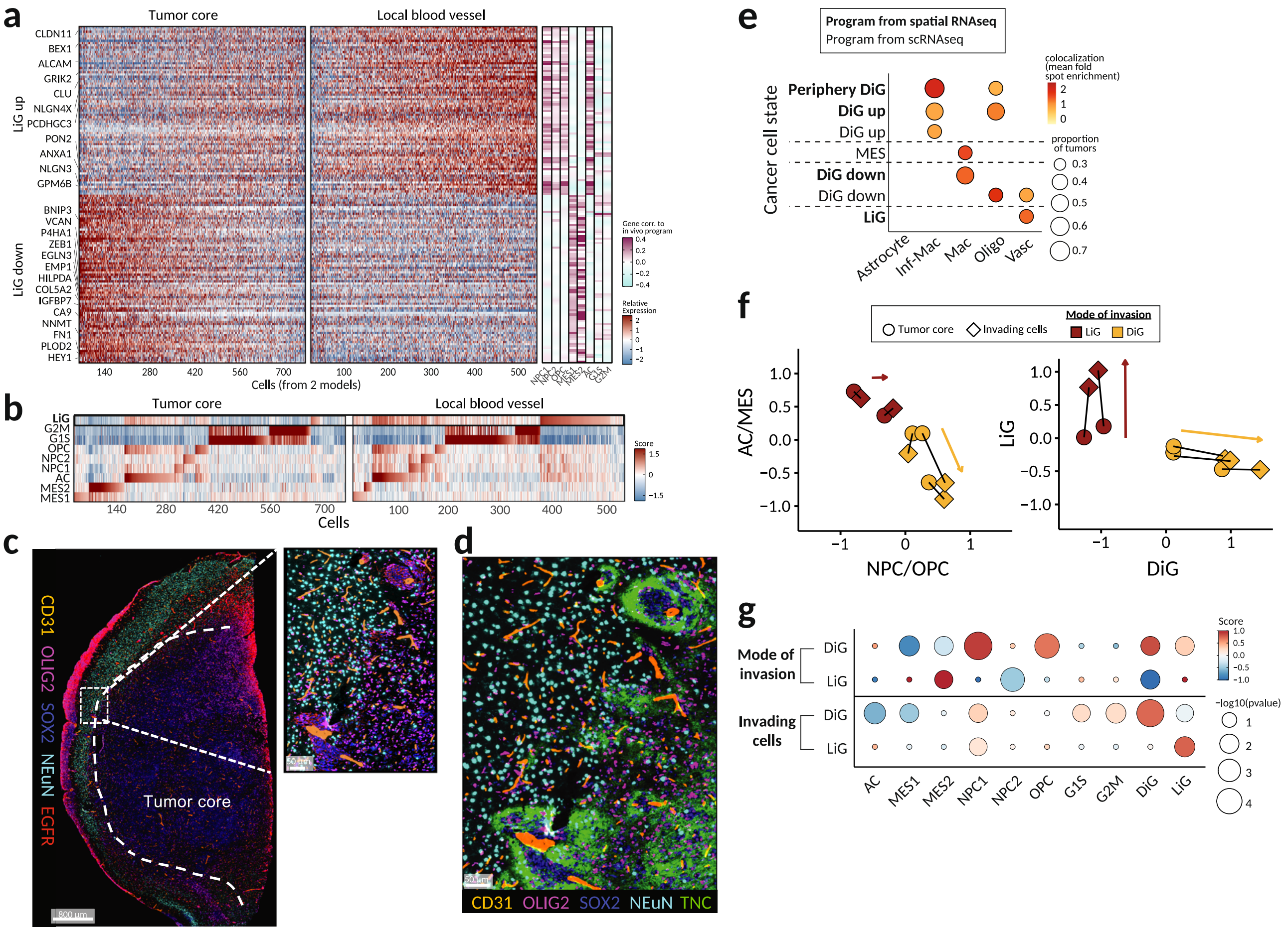

Fig. 4 | Profiling locally invading cells. a Main heatmaps show the expression of LiG program genes (bottom: downregulated, top: upregulated) in the tumor core cells (left) and blood vessel invading cells (middle). Heatmap on the right shows the correlation of each gene to the average expression of each of the GBM metaprograms from Neftel et al. **b** Heatmaps show scores for the GBM metaprograms from Neftel et al. and LiG (top) for cells from the tumor core (left) or blood vessel invasive cells (right). **c** Representative CODEX image among three models profiled of the ipsilateral hemisphere showing glioma cells (SOX2+) with local invasion along blood vessels (CD31+) and upregulation of AC-OPC markers (EGFR+, OLIG2+). **d** Representative CODEX image, among three models profiled, of the ipsilateral hemisphere showing glioma cells (SOX2+) with local invasion along blood vessels (CD31+) and deposition of the glioma specific ECM glycoprotein tenascin-C (TNC). **e** Heatmap shows spatial associations between TME cell types (X-axis) and different cancer cell states (Y axis), where the color of the circle is the mean spot fold enrichment and the size of the circle represents the proportion of tumors that the association is found in. Programs derived from spatial data are in bold font. **f** Scatterplots show the average scores for invading cells (diamond) and tumor core cells (circle) for NPC/OPC (X-axis) against AC/MES (Y-axis) (left) or spatial DiG (X-axis) against LiG (Y-axis) (right) per tumor, where a matched pair is connected by a line. The points are colored by the type of invasion, where LiG is red and DiG is in yellow. Arrows are scaled in the average direction of primary to invasion across models per mode of invasion. **g** Heatmap shows the associations of the Neftel cell states, cell cycle states, and invasion programs (x axis) with various invasion features. Colors represent the relative value and size of the circle is proportional to the -log10(p-value) of each comparison. Top: Mode of invasion is defined as the average score for DiG models (top, GS143, L0627, L0104) and LiG models (bottom, MGG123, MGG65) vs all other samples. Bottom: Cells undergoing invasion are defined by the difference in average score in invading cells in DiG models (top) or LiG cells (bottom) vs tumor core cells. The significance (dot size) reflects comparisons determined by a two-sided Paired Student's t-test (for Invading cells: Primary vs. Invasion within models) and a two-sided unpaired Student's t-test (for Mode of Invasion: DiG vs. LiG). Source data are provided as a Source Data file.

when the cells detach from the bulk of the tumor and move into completely different niches, with an altered milieu of interacting cells and other tissue components. Accordingly, DiG and LiG reflect unique signatures, with only partial associations to predefined cell states. Therefore, the previously defined Neftel cell states can consistently distinguish models favoring distal *vs.* local invasion (Fig. 4f left and 4g top), but the unique invasion states more effectively distinguish the invasive *vs.* non-invasive cells within a model (Fig. 4f right and 4g bottom). While the spatial DiG state captures cancer cells actively invading along white matter tracts, once cancer cells have traversed the corpus callosum or the anterior commissure, they may also invade along blood vessels where they upregulate ECM markers (TNC, HPLN1) in addition to neurodevelopmental lineage markers (SOX2, OLIG2) (Figure. S4E), consistent with the role of ECM remodeling in vascular invasion[33].

Mapping the TME of GBM invasion

Having defined distinct transcriptional programs associated with GBM invasion, we next sought to characterize the TME and spatial context of invasion along these routes. Using both spatial transcriptomics and CODEX, we explored how malignant invasion states are embedded within, and potentially shaped by, their local environment. We first examined the anatomical distribution of the malignant invasion states. Several location-dependent associations between malignant invasion states and anatomically-defined neuronal subsets emerged. For example, the core spatial DiG state was most associated with subsets of inhibitory neurons in close proximity to white matter tracts, whereas distant DiG was most associated with cortical excitatory neurons (Figure. S5a–d, **Methods**).

Next, we asked whether non-neuronal components of the TME differ between the ipsilateral (tumor core) and contralateral (distal invasion) hemispheres. We observed two consistent differences between the ipsilateral and contralateral TMEs: a shift in glial cell composition from more astrocyte-abundant ipsilateral TME to more oligodendrocyte-abundant contralateral TME ($p = 0.03$), and a shift in myeloid composition from a canonical GBM macrophage/microglia program (Mac) (e.g., *Apoe, Trem2*) to an inflammatory macrophage/microglia program (Inf-Mac) (e.g., *Ccl2, Ccl4*) ($p = 0.02$, Fig. 5A). In distally invasive tumors, we observed recruitment of F4/80+, P2y12+ myeloid cells to cancer cells invading through the contralateral hemisphere (Fig. 5b). In contrast, myeloid cells of the tumor core were F4/80+ while myeloid cells in the gray matter were P2y12+ only. This aligns with recent work showing that microglia are mobilized ahead of invasion, guiding GBM migration along invasion routes[45]. Accordingly, DiG cancer cells were significantly colocalized with Inf-Mac, while LiG cancer cells were significantly associated with endothelial cells and pericytes (Vasc) (Figs. 4e and 5c).

The enrichment of Inf-Mac in the contralateral hemisphere and its spatial association with DiG cancer cells led us to examine further the differences between cancer-associated macrophages in the two hemispheres. Apart from Inf-Mac genes, contralateral macrophages also upregulated OXPHOS-related genes, while downregulating canonical macrophage genes, with no changes in the expression of microglial genes (e.g., *Cx3cr1, Selplg*), indicating they are distinct from the dominant myeloid populations of the tumor core and the normal brain (Fig. 5d and Figure S5e, f). Interestingly, cancer cells in the contralateral hemisphere that were coupled to Inf-Mac also upregulated OXPHOS-related genes, as well as *GPX4*, a member of the glutathione peroxidase family, which protects cells from oxidative stress[46] (Figure S5f, g).

We additionally inferred interactions between distally invasive malignant cells with neurons, and between peri-vascular invading malignant cells with endothelial cells (Methods), identifying ligand-receptor pairs upregulated by invading cancer cells and their interacting TME counterparts (Figure S5h–j). For example, interacting endothelial cells and invading cancer cells upregulated ECM-related gene pairs such as Ptn-SDC3, Fn1-ITGAV, and Bcan-EGFR.

Collectively, we resolved GBM invasion at three levels of granularity (Fig. 5e): First, malignant features associated with overall invasion capacity *between* models; second, malignant features associated with specific modes of invasion *within* models; and third, malignant features within those modes of invasion that reflect specific associations with the TME. Importantly, the expression patterns associated with each level of invasion are distinct.

Discussion

Locally and distally invasive GBM cells are responsible for recurrence in the majority of patients and pose a significant challenge, yet we lack a comprehensive understanding of such cells. We found that the efficiency of distal invasion correlated with the fraction of OPC-like cells in each model, supporting the potential role of OPC-like cells in distal invasion and possibly mirroring the migratory capability of normal OPCs during development. Next, we showed that models without detectable distal invasion and with a MES-like expression profile may exhibit local peri-vascular invasion. These results suggest that multiple cellular states are associated with effective invasion capacity, and that distinct states are predisposed for invasion along different routes[47], possibly accounting for the widespread invasion phenotypes seen in patients.

Importantly, in both routes of invasion, invading cells are associated with unique signatures that we identified by scRNA-seq and then validated by ST. These signatures distinguish the invading cells from cells of the same model that are found in the tumor core, highlighting the distinction between cell states linked to the propensity for invasion from those associated with the process of invasion. The propensity for invasion is primarily linked to cell states such as OPC-like and MES-like that represent the dominant patterns of heterogeneity within tumor cores and hence were previously described[16]. In contrast, ongoing invasion is linked to the activation of signatures that are less abundant in tumor cores and, therefore, were not identified by single-cell analysis of bulk tumors. Such invasion signatures may reflect the expression changes that occur in cancer cells as they move from a tumor microenvironment to the brain parenchyma, thereby modulating their cell-cell interactions, cell-matrix interactions, and their nutrient and oxygen availability. While our findings delineate distinct route-specific invasion programs (LiG vs. DiG), these states may also represent different points along a dynamic temporal progression, potentially sharing core mechanisms that are adapted to the immediate anatomical niche.

For example, we identified unique associations between distally invading cancer cells and their TME, such as their association with inflammatory myeloid cells. Inflammatory myeloid cells, as well as the subset of cancer cells in the contralateral hemisphere that were directly associated with them, both upregulated OXPHOS, which may represent a metabolic adaptation to the invasive niche, similar to some metastases[48–50]. Additional work will be needed to better understand the mechanisms that activate invasion signatures and their potential relevance in modulating the ability of cells to invade.

In other cancers, numerous studies implicated epithelial-mesenchymal transition (EMT) in invasion and metastasis. For example, EMP1, which we found to be downregulated in distally invasive models and among invasive cells, was recently shown to drive metastasis in colorectal cancer[51], highlighting the unique and often opposing features of invasion in GBM compared to other cancers. The diffuse invasion of tumor cells within the brain might be constrained by brain-specific structures, such as the white matter tracts and blood vessels, requiring tumor cells to adapt to and infiltrate local environments. In line with this, GBM invasion has been described to mimic non-malignant brain cells during embryonic development, as well as adult stem cells in the mature brain[9].

Traditionally, the prevailing belief was that cellular migration and invasion necessitate a transition from a proliferative to an invasive state[52]. These concepts are rooted in studies on EMT in development and epithelial cancers. For instance, Snail, an EMT-related transcription factor, has been shown to suppress the cell cycle[53]. However, our findings reveal a positive association between distal invasion and the cell cycle, in line with a recent in vivo optical imaging study[41]. Since distal invasion is associated with OPC-like cells, this may reflect the combined proliferative and migratory features of normal OPCs. Accordingly, invasion phenotypes may differ between cancer types, perhaps reflecting the unique biology of the developmental programs that are co-opted in each cancer context.

In summary, through scRNA-seq and spatial analysis of invasive cells in GBM PDXs, we show that the route of invasion and the ongoing process of invasion are both linked to specific tumor cell states, including previously defined states as well as invasion-associated states. This consistent association with invasion phenotypes may suggest that modulation of cell states could potentially prevent invasion and could be imperative for achieving recurrence-free therapeutic outcomes.

Methods

Ethical statement

In vivo experimental procedures were approved by the Institutional Care and Use Committee (IACUC) at Massachusetts General Hospital (2019N000229) and the University of Michigan (PRO00011658) and were performed in accordance with institutional regulations.

GBM spheroid culture

Patient-derived human glioblastoma cells[19,54,55] derived under IRB #2005P001609 were maintained on a low-attachment surface (Corning)

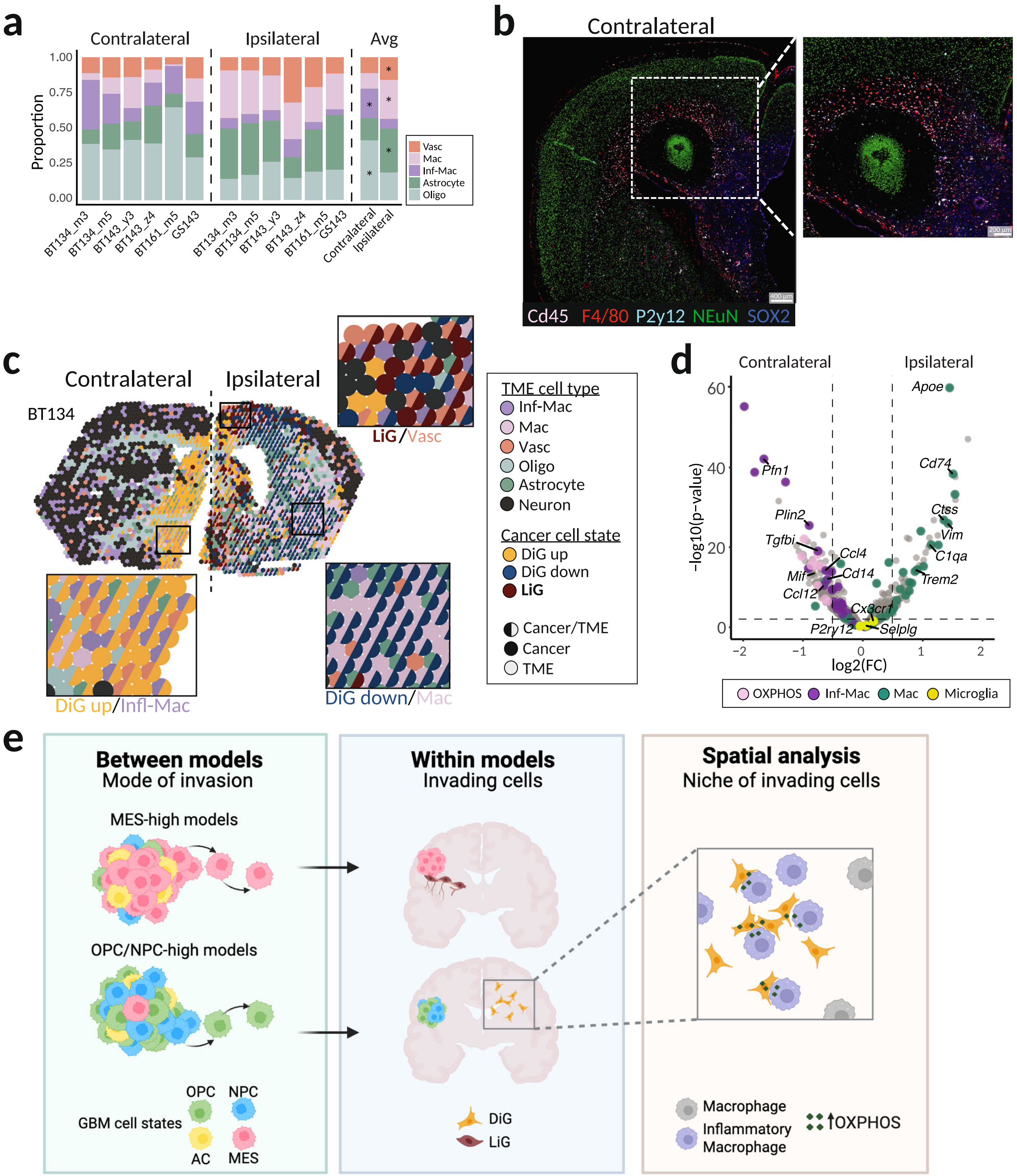

Fig. 5 | Tumor microenvironment associations in invading cells. **a** Barplots show the quantification of proportions of TME cell types in contralateral (left) and ipsilateral (right) hemispheres across 6 Visium samples. **b** Representative CODEX image showing myeloid recruitment (F4/80+, P2y12+, CD45+) to the white matter tracts, alongside invading SOX2+ cancer cells, in the contralateral hemisphere in PDX model L627. Neurons (NEuN) are in green. **c** Spatial map shows spots colored by the TME cell types or malignant invasion programs. Spots that are mixed between TME and cancer are colored by both nonmalignant cell types and malignant cell states. In all panels, cell states defined from the spatial data are in bold. **d** Volcano plot shows the differentially expressed genes between macrophage spots in contralateral vs ipsilateral hemispheres. Colored spots correspond to Inf-Mac (purple) and Mac (green) programs, microglia genes (yellow), or OXPHOS genes (pink). Differential expression was determined using a two-sided Student's t-test, with *p* values adjusted for multiple comparisons using the Benjamin-Hochberg procedure (FDR). **e** This scheme illustrates how glioblastoma (GBM) cell states influence the mode of invasion. (Left) MES-high tumors correlate with local invasion, whereas OPC/NPC-high tumors are linked to distal invasion. (Center) These distinct invasion patterns are driven by specific cell programs: (LiG and DiG cells). (Right) A spatial analysis of the DIG niche reveals a unique microenvironment enriched for inflammatory macrophages and OXPHOS. Created in BioRender. Chanoch-Myers R. et al. (https://BioRender.com/bim1q9w).

with Neurobasal Medium (Thermo Fisher Scientific) supplemented with 1/2 x N2 and 1 x B27 (Thermo Fisher Scientific), 1% Penicillin/Streptomycin (Thermo Fisher Scientific), 1.5 x Glutamax (Thermo Fisher Scientific), 20 ng/mL of EGF and 20 ng/mL of FGF2 (Shenandoah Biotechnology). Prior to multiplexed in vivo xenograft experiments, GBM spheroid models were cultivated in T75 flasks separately and were profiled by scRNA-seq as described below. Subsequently, 10 GBM spheroid models were mixed (1.5 × 105 cells each) in 6 well plates, grown for 48 h, snap labeled with CMV-N16-GFP lentiviral vector for 24 h before harvested for stereotaxic injection. A portion of cells was further maintained in culture for 48 h, and analyzed by flow cytometry to determine the efficiency of the viral labeling and cell viability.

Experimental mouse model

Healthy, naive female NOD.Cg-Prkdc <scid > IL2rg <tm1Wjl > /SzJ (NSG) mice aged 6-8 weeks were purchased from the Jackson Laboratory (Bar Harbor, ME). All mice were housed in specific pathogen-free conditions. Housing rooms employ centrally controlled and monitored light cycles that utilize a 12-h light / 12-h dark photoperiod. Individual room has remote temperature setpoint adjustment and maintained within plus or minus 2 degrees throughout a range of 18 − 26 C. Relative humidity within the animal suite is maintained at 30–70%. Stereotaxic injections were performed as described previously[19,37,56]. Briefly, cells (1.5 × 105 cells for multiplexed experiment; 10^5 for single-model injection) resuspended in 1 uL PBS were loaded on a Hamilton syringe with 26-gauge needle, and injected at a speed of 0.1uL/30s-1min using the following coordinate: 0 mm posterior, 2.5 mm lateral, and 2.5 mm dorsal to the bregma. Upon completing injection, the needle was left in place for 3 min, then withdrawn slowly in 2 min to help reduce virus reflux. In this study, tumor size or burden was not used as a criterion for endpoints because the tumors were grown intracranially and were not externally visible. Endpoints were instead determined based on IACUC-approved (2019N000229) clinical symptoms caused by the growth of intracerebral tumors, such as significant body weight loss (20% or more weight loss from baseline weight), seizures lasting more than 10 seconds (seizures involving blank stares or shaking will both be considered), or a persistent hunched posture with diminished activity.

Statistics & reproducibility

No statistical method was used to determine sample sizes. The number of cells injected and profiled was determined empirically. GBM spheroids were pooled for the above-described multiplexed in vivo assays without regard to spheroid identity, but experiments were not randomized. No data were excluded from the analysis, except for individual cell and spatial spot data points that did not pass quality control. Mouse brain tissue collection, processing, and single-cell data generation were performed without the knowledge of model identity. During data analysis, the identities of GBM spheroids used to generate transcriptome data were not blinded.

Isolating invading cells and tumor cores in GBM PDXs

Mice were euthanized upon reaching pre-determined clinical endpoints such as significant body weight loss, seizures, and a persistent hunched posture with diminished activity. The collected mice brains were imaged with a fluorescent stereomicroscope with 0.63 objective magnification (Olympus MVX10, Leica M205), which covers both the entire brain and cell morphology at single-cell resolution. Under the microscope, the brains were observed from the ipsilateral hemisphere for tumor-peripheral invasion to the contralateral hemisphere for distal invasion. For distal invasion, the tumor cores were dissected from the ipsilateral hemispheres, centered around the injection site, identified by the hole created during stereotaxic injection, and based on GFP intensity, ensuring the removal of GFP-negative outer surface of the brains. Contralateral samples were collected from the hemisphere opposite the injection site, avoiding the midline border regions (approximately 500 µm). During dissections of the contralateral hemispheres, we observed lower and more restricted GFP signals compared to the ipsilateral hemisphere. For local blood vessel-associated invasion, tube-structured GFP+ cell clusters were dissected under a stereomicroscope without introducing any bulk tumor mass. Then, samples from each location were mechanically and enzymatically dissociated using a papain-based neural tissue dissociation kit (Miltenyi Biotec) supplemented with 0.1% Type I collagenase (Thermo Fisher Scientific)/PBS. The dissociated cells were first stained with calcein Blue AM (BD Biosciences) and Zombie NIR (BioLegend) for 25 min at 4 C, and with anti-mouse CD16/32 (BD Biosciences) for 5 min. After washing cells with ice-cold 1% BSA/PBS, the cells were then stained with PerCP anti-mouse CD45 (clone 30-F11, BD Biosciences) for 30 min at 4 C. Sorting was performed with Becton Dickinson Influx cytometer (Becton Dickinson). Side scatter (SSC) width versus forward scatter (FSC) area and Trigger Pulse Width versus FSC criteria were used to discriminate doublets and gate-only singleton cells. Viable single cells were identified as calcein blue AM positive and Zombine NIR negative to low cells. We sorted viable CD45 negative/GFP positive cells from blood-vessel associated invasion samples into 96-well plates containing 10uL of TCL buffer (QIAGEN) with 1% beta-mercaptoethanol (Sigma Aldrich). Plates were frozen immediately after sorting and stored at −80 degree prior to whole transcriptome amplification, library preparation, and sequencing. For multiplexed samples, CD45 negative/GFP positive cells were sorted into 15 mL tumors for subsequent 10X scRNA-seq processing.

Single cell RNA-sequencing

Smart-seq2 whole transcriptome amplification, library construction, and sequencing were performed as previously published[16]. The spheroid models in vitro were processed as a pool using TotalSeq-B/Hashtag anti-bodies (BioLegend), described previously[19]. Each of the dissociated cells was first stained with HumanTruStain FcX (BioLegend) in Cell Staining Buffer (BioLegend) for 10 min at 4 C, and then stained with barcoded TotalSeq-B anti-bodies targeting human CD298 and b2 microglobulin in a separated tube for 30 min at 4 C. We generated a single cell suspension of the pool in 0.04% PBS-BSA and loaded approximately 9900 single cells to the Chromium Controller with a targeted recovery of 6000 cells. Single cells, reagents and single gel beads containing barcoded oligonucleotides were encapsulated into nanoliter-sized droplets and subjected to reverse transcription. Droplets were broken and the barcoded cDNAs were purified with DynaBeads and amplified by 12 cycles of PCR (98 C for 3 min; [98 C for 15 s, 63 C for 20 s, 72 C for 1 min] × 12; 72 C for 1 min). Gene expression cDNA and TotalSeq antibody derived barcode cDNA were size-selected and separated with SPRIselect Reagent (Beckman Colter), and then fragmented, end-repaired, ligated with index adaptors. Quality control of the resulting libraries was performed with the Bio-analyzer High Sensitivity DNA Analysis (Agilent). The constructed gene expression library and barcode library were combined at 4:1 ratio and sequenced with paired-end, 28 and 55-base reads, using a NextSeq 2000 sequencer (Illumina).

Single cell RNA-sequencing data processing

Data was used in transcript-per-million (TPM) or UMI count matrices. As quality control, we excluded cells with fewer than 2000 detected genes. For TPM matrices, expression levels were quantified as E(I,j) = log2(TPM(i,j)/10 + 1), where TPM(i,j) refers to transcript-per-million for gene i in cell j, as quantified by RSEM[57]. The average number of transcripts detected per cell was less than 100,000, thus TPM values were divided by 10, to avoid inflating the differences between detected (E(i,j) > 0) and non-detected (E(i,j) = 0) genes, as previously described[58]. For UMI count matrices, expression levels were quantified as E(i,j) = log2(1 + CPM(i,j)/10), where CPM(i,j) refers to 106∗UMI(i,j)/ sum[UMI 1..n,j], for gene i in sample j, with n being the total number of analyzed genes. CPM values were divided by 10, as described above for TPM values. We defined relative expression over the remaining cells for each study separately, by centering the expression levels per gene, $Erel(i,j) = Ei,j--mean[Ei,1...n]$. Next, we calculated the $Eavg(i) = log2(mean(CPMi,1...n)+1)$ for each gene, and excluded genes with Eavg <4. The gene-cell matrix underwent dimension reduction using UMAP and Louvain clustering using the R package Seurat (https://satijalab.org/seurat/).

Definition of gene signature scores

Cells or bulk tumors were scored for a gene signature as previously described, using the R package scalop (https://github.com/jlaffy/scalop). Given a set of genes (Gj) reflecting an expression signature of a specific cell type or biological function, we calculate for each cell i, a score, SCj (i), quantifying the relative expression of Gj in cell i, as the average relative expression (Er) of the genes in Gj, compared to the average relative expression of a control gene-set (Gj cont): $SCj (i) = average[Er(Gj,i)]-average[Er(Gj\ cont,i)]$. The control gene-set is defined by first binning all analyzed genes into 30 bins of aggregate expression levels (Ea) and then, for each gene in the gene-set Gj, randomly selecting 100 genes from the same expression bin. In this way, the control gene-set has a comparable distribution of expression levels to that of Gj, and the control gene set is 100-fold larger, such that its average expression is analogous to averaging over 100 randomly selected gene-sets of the same size as the considered gene-set. Cells were scored for each study separately.

Determining the identity of GBM models in multiplex experiment

First, we applied an expression-based method to assign cells from each multiplexed PDX to the individual spheroids we profiled by scRNA-seq separately, similar to the method previously described[36]. In this approach, we generated model-specific signatures for each spheroid using in vitro scRNA-seq data from all of the injected models. The signatures were defined as the top 50 most differentially expressed genes when comparing each model to the remaining models. Next, we clustered the cells from each multiplex pool group using Louvain clustering. We scored each cluster for the model-specific signatures, where clusters with high overall similarity (> 0.5) for the model scores were combined. Clusters were assigned by their cluster's average score for the signatures.

Next, we applied the SNV-based classification using souporcell[34] to identify the unique genotypes for each model grown in vitro. We then applied this same method to our multiplex PDX pools. The algorithm was used with the parameter to identify 10 clusters because we had originally injected a pool of 10 models into each mouse. After grouping individual genotype clusters with high overall correlation (> 0.5), we correlated clusters with the in vitro genotypes using Demuxafy[35] to classify the model identity of each cluster. Finally, a consensus classification approach, combining the expression-based and SNV-based methods, was used to identify PDX models.

Comparing invasive and non-invasive models

We determined each model's invasion capability based on the presence of cells from that model in the invasive site (contralateral hemisphere) of the multiplex experiment. Next, we generated pseudobulks of the tumor cores for each cell line from the scRNA-seq multiplex experiment. In addition, we combined these pseuduobulks with a previously published dataset of GBM PDXs profiled by RNA-seq and annotated for their invasion capability (Invasion Score between I and IV[32]) and compared the expression of tumors that were invasive (Invasion Score of III-IV or models with invasion detected in our experiment) to those that were noninvasive (Invasion Score of I-II or models with no invasion detected in our experiment).

Characterization and comparison of invasion programs to human metaprogram states

The invasion programs were defined as the top 75 differentially expressed genes between invasive cells and tumor core cells that were conserved across models in either distal invasion (DiG) or local invasion (LiG). For both invasion programs identified, we calculated the Jaccard similarity with each of the previously defined human metaprograms[16] and other invasion related signatures. In addition, we calculated for each gene in each program, the correlation of its expression with the average expression of the canonical human GBM metaprograms defined in Neftel et al. 2019.

Ligand-receptor interaction analysis

To investigate potential cell-cell communication pathways, we performed a ligand-receptor interaction analysis as previously described[19]. We focused on identifying interactions between invading malignant cells (DiG or LiG populations) and the specific non-malignant cells that constitute their respective tumor microenvironment niches: neurons for DiG cells and endothelial cells for LiG cells. Ligand and receptor expression was assessed in our invading cell populations. We then queried for corresponding receptor and ligand expression within a publicly available single-cell RNA-sequencing dataset of non-malignant cells from human GBM tumors[59,60]. A ligand-receptor pair was considered a potential interaction if the ligand was expressed in one cell population and its cognate receptor was expressed in the other, as previously explained in Hara et al. This approach allowed us to map the potential communication networks between invading cancer cells and their niche-specific stromal partners.

Pseudotime trajectory analysis

To infer developmental trajectories and order cells along a continuous path, we performed pseudotime analysis using the slingshot R package[61]. A low-dimensional embedding of the cells from each invasive models separately was first generated via principal component analysis (PCA) on the normalized gene expression data for each model. The slingshot algorithm was then applied to this PCA embedding to identify the principal cellular trajectory and assign a pseudotime value to each cell, representing its progress along the inferred developmental continuum. To identify gene programs associated with this trajectory, we used the R package tradeSeq[62]. From this analysis, we identified three distinct programs in each model that were significantly correlated with pseudotime.

Tissue immunostaining

Collected PDX samples were fixed with 2% PFA in PBS for 16 h at 4 °C and then stored in PBS until further processing. Thick 100um brain floating sections were prepared with a vibrating blade microtome (Leica VT1000 S) and stored in tissue freezing media (25% Glycerol, 30% Ethylene glycol, 1.38 g/L $NaH2PO4$, and 5.48 g/L $Na2HPO4$) at −20 °C. Sections were blocked with 10% Goat serum and 0.3% TritonX-100 in PBS for 2 h and immunostained for brain endothelium using anti-CD31 (MEC13.3; BD Biosciences) antibody overnight at 4 °C, followed by secondary antibody AF647 anti-rat IgG (Invitrogen) for 2 h at room temperature and DAPI for nucleus staining. The images were acquired with laser-scanning confocal microscopy (Zeiss).

CODEX (multiplexed imaging)

The antibody panel was designed to capture the human and murine cell types and states of interest (Supplementary Data S5). With the exception of the pre-conjugated CD31 antibody from Akoya, all antibodies were validated by conventional immunofluorescence on control tissues, including human glioblastoma and mouse control brain samples. For validation, fresh-frozen sections were fixed in 4% paraformaldehyde (20 min), blocked with 4% BSA and 0.25% Triton X-100

(30 min), incubated with primary antibodies overnight at 4 °C, and subsequently with secondary antibodies for 2 h at room temperature. All antibodies were further validated post-conjugation in control samples using multiple CODEX runs, allowing adjustment of antibody concentrations and exposure times to optimize signal-to-noise ratios. CODEX experiments were performed on the PhenoCycler-Fusion and imaged on the PhenoImager (Akoya Biosciences) following the manufacturer's instructions.

Visium Sample Preparation

Samples were flash frozen by liquid nitrogen and embedded in cold OCT on dry ice (Scigen OCT Compound, #4586). The RNA quality of each sample was evaluated by Tapestation (Tapestation RNA Screen Tape, Agilent) following RNA isolation (Zymo Quick RNA MicroPrep Kit, #ZR-R1051). Fresh frozen samples were sectioned at 10um thickness with a cryostat onto 10X Visium Spatial Transcriptomics slides (Visium Spatial Gene Expression Slide and Reagent Kit, PN-1000184) according to the manufacturer's instructions.

Visium H&E staining and imaging

Tissue sections on Visium slides were first fixed in methanol (Millipore Sigma #34860) followed by an aqueous eosin-based H&E protocol according to manufacturer's instructions (10X Visium Methanol Fixation, H&E Staining, and Imaging Protocol CG000160). Brightfield imaging was performed using a wide-field Leica DMIi8 inverted microscope (Leica-microsystems CMS GmbH Germany) equipped with a DFC310FX color camera. Images were acquired with a 10x/0.25 dry objective and stitched by Leica Application Suite X software. Image post-processing was performed with Fiji version 2.3.1.

Visium cDNA synthesis and library generation

Following imaging of H&E staining, permeabilization (9 minutes, as determined by Visium tissue optimization experiment) was carried out on the Visium slide to capture mRNA released from the tissue. cDNA synthesis and library generation were performed with the Visium Spatial Gene Expression Slide and Reagent Kit (10X Genomics). Quality control and quantification of the resulting dual-indexed barcoded libraries were performed with Agilent TapeStation and by qPCR (NEBNext Library Quant Kit for Illumina, New England Biolabs).

Tissue preparation and sectioning for Visium HD

Brains from GS143 PDX models were extracted and fixed with 10% formalin for 16–24 h at room temperature, then switched to 70% ethanol. Paraffin blocks were generated and adjacent or near-adjacent 5 μm sections were taken from the FFPE tissue blocks following the Visium HD FFPE Tissue Preparation Handbook (CG000684, Revision B).

RNA quality assessment for Visium HD

RNA quality was assessed by scraping off two adjacent 5 μm sections, performing tissue slide deparaffinization (Qiagen, cat #19093), extracting RNA following the AllPrep DNA/RNA FFPE Handbook (Qiagen cat #80234) and calculating the DV200 score. Briefly, mean RNA fragment size is a reliable indicator of RNA quality. As such, the percentage of total RNA fragments >200 nucleotides (DV200) were measured for RNA quality assessment upstream of library preparation. Following the recommendation of the Visium HD FFPE Tissue Preparation Handbook (CG000684, Revision B), tissues were used with the Visium HD Spatial Gene Expression if they had a DV200 of >30%.

Visium HD cytassist spatial gene expression for FFPE

5 μm sections were cut from previously mentioned formalin-fixed paraffin-embedded blocks and mounted onto Visium HD Cassettes. H&E staining and imaging were performed following the Visium HD FFPE Tissue Preparation Handbook (CG000684, Revision B). Samples were then processed and sequenced following the Visium HD Spatial Gene Expression Reagent Kits User Guide (CG000685, Revision B). Briefly, the region of interest in the slides was subjected to heat- and solvent-mediated deparaffinization, decrosslinking, and tissue permeabilization. Probe hybridization, ligation, and probe extension were carried out on-slide to capture transcriptomic information while preserving spatial architecture. Following second-strand synthesis and cDNA amplification, libraries were prepared according to the Visium HD protocol, indexed, and sequenced on an Illumina platform following the Visium HD Spatial Gene Expression Reagent Kits User Guide (CG000685, Revision B) to generate spatially resolved transcriptomic profiles.

Visium Sequencing

Final library QC was performed by Tapestation. Pair-end dual-indexed final libraries were diluted to 1.8 nM, pooled, and denatured prior to sequencing on Novaseq (Illumina) using the Novaseq SP 100 cycles sequencing kit (Illumina) with 1% PhiX and the following sequencing parameters: Read 1 – 28 cycles, Read 2 – 90 cycles, Index 1 – 10 cycles, Index 2 – 10 cycles.

Visium Alignment and data pre-processing

Alignment of FASTQ files to a concatenated human (GRCh38) and mouse (mm10) transcriptome (GRCh38-mm10-2020A), UMI counting, and spot barcode filtering were performed using SpaceRanger (version 1.1, 10X Genomics). Alignment between positionally barcoded Visium spots and tissue images to obtain spatial coordinates necessary to generate spatial maps was performed using Loupe Browser (version 5.0.1, 10x Genomics). Expression levels were quantified (separately for mouse and human genes) as Ei,j = log2 (1 + CPMi,j/10), in which counts per million (CPM)i,j refers to 106 × UMIi,j/sum(UMI1…n,j), for gene i in sample j, with n being the total number of analyzed genes. The average number of UMIs detected per spot was less than 100,000; thus, CPM values were divided by 10 to avoid inflating the differences between detected (Ei,j > 0) and undetected (Ei,j = 0) genes as previously described[58].

For each spot, the number of counts was used as a proxy for sample quality. Spot QC filtering was performed separately for mouse and human reads. For each species, spots with fewer than 500 counts and/or expressing more than 10% mitochondrial genes, another proxy for low quality, were filtered out. For mouse and human separately, the top ~7000 most highly expressed genes were retained, and centering was performed per sample in order to define relative expression values by subtracting the average expression of each gene i across all k spots: Eri,j = Ei,j − average(Ei,1…k), where Er represents relative expression values.

Five GBM PDX Visium mouse brains (spanning four invasion models) that were profiled by Manoharan et al[42]. were included in our analysis (Supplementary Data 4). The same QC filtering and pre-processing were performed. No batch integration was required since our analysis is generally performed per sample, and only the results of various analyses are combined across samples.

Segmentation by hemisphere

In some cases, an entire brain was sectioned onto a single Visium capture area. Therefore, in order to perform analysis comparing the ipsilateral (tumor core) and contralateral (invading) hemisphere, it was necessary to assign all tissue-covered spots to a hemisphere. We performed segmentation and annotation of the hemispheres using the "createSegmentation" function in the SPATA2 R package, which provides a GUI for manual segmentation and then returns a vector of spot assignments based on the segmentation[63].

Scoring and annotating Visium data by malignancy fraction and by single-cell invasion programs

First, the malignancy fraction of each spot was inferred by the ratio of human/mouse reads. Second, spots could be further binned as

"Cancer," "TME," and "Mixed" based on the distribution of human/mouse reads. Spots were then scored for the single-cell invasion programs (using only human reads) using the scalop R package (https://github.com/jlaffy/scalop) as previously described[16]. Given a set of genes (Gj) reflecting an MP corresponding to a cell state or cell type, we calculate for each spot i, a score, SCj(i), quantifying the relative expression of Gj in spot i, as the average relative expression (Er) of the genes in Gj, compared to the average relative expression of a control gene set (Gj cont): SCj (i) = average[Er(Gj,i)] − average[Er(Gj cont,i)]. The control gene-set is defined by first binning all analyzed genes into 30 bins of aggregate expression levels (Ea) and then, for each gene in the gene set Gj, randomly selecting 100 genes from the same expression bin. In this way, the control gene set has a comparable distribution of expression levels to that of Gj, and the control gene set is 100-fold larger, such that its average expression is analogous to averaging over 100 randomly selected gene sets of the same size as the considered gene set.

Spots were annotated for the spatial DiG program based on the difference between the spatial DiG program and the DiG program. Annotation thresholds were then set based on the distribution of the differences, where a spot was classified as "spatial DiG" if the difference between the scores was >=0.5. For spot annotation to Neftel states and other malignant programs, spots were assigned to the program for which it scored most highly with a minimum difference of at least 0.2 between the highest-scoring program and the second highest-scoring program.

Defining malignant signatures from spatial data

In addition to annotating the Visium PDX data by the single-cell derived invasion programs, we also performed unsupervised analysis to derive malignant signatures directly from the spatial data in several different ways using only the human (i.e., malignant) genes and expression data. First, we considered differentially expressed genes (DEGs) between the ipsilateral and contralateral hemispheres per model. We then derived consensus signatures for ipsilateral and contralateral malignant programs based on the recurring DEGs across models. Second, we defined gene signatures based on DEGs between malignant spots colocalized with a specific TME cell type (for example, vascular or macrophage) and malignant spots not colocalized with a specific TME cell type. Third, we derived consensus gene signatures as previously described[28]. Briefly, for each sample (using only human reads), Leiden clustering was performed on the SNN graph (implemented with Seurat version 4.3.0). Per sample gene programs were defined per Leiden cluster by differential expression analysis based on the top 50 most differentially expressed genes by the Wilcoxon Rank Sum Test with a p value of <0.005. The per sample gene programs were then clustered based on their Jaccard similarity and consensus gene signatures were defined from the top 50 recurring genes per cluster as defined by Jaccard similarity.

Defining nonmalignant cell type signatures from Visium data

In order to annotate spots by their dominant TME cell type, we first redefined single-cell and spatial nonmalignant TME cell type signatures from the Visium PDX data as follows: spots were scored for the original signatures (mouse reads only). Genes were retained in the cell type signature if they had a correlation >0.2 with the overall program score for that signature.

Next, we derived consensus signatures for neuronal subsets/anatomical locations. First, we generated per sample Leiden-derived gene programs as described above. Second, we performed NMF on each sample separately to capture continuous patterns of gene expression variation, as previously described[28]. Negative values in each centered expression matrix were transformed to zero. To minimize the influence of selection of an individual k parameter, we ran NMF with multiple k values ranging from 2-11. Each NMF program was summarized by the top 50 genes based on NMF score. Consensus signatures corresponding primarily to neuronal subsets and anatomical locations were derived by jointly clustering per sample NMF and Leiden gene programs collected from all samples by their Jaccard overlap and selecting the top 50 most recurrent genes across samples per cluster. Finally, in several cases where we observed clear subclusters within a cluster, we then performed hierarchical clustering, which resulted in further splitting neuronal clusters to additional subclusters.

Spots were given two TME annotations: one based on the dominant non-neuronal TME score (i.e., Mac, Oligo, Astrocyte, Inf-Mac, or Vasc) and an additional annotation based on neuronal subtype/anatomical location). For each annotation category, in order for a spot to be assigned to a given program, the spot needed to score at least 0.25 higher for that program than any other program.

Colocalization and spot enrichment analysis

For colocalization between malignant states and nonmalignant cell types, only mixed composition spots (defined as at least 20% malignant and 20% nonmalignant) were considered. First, p values (calculated by hypergeometric test) and fold-enrichment values (defined as observed colocalization/expected colocalization) were calculated per sample. Finally, a mean fold-enrichment value for each pair of cell states/cell types across all samples and effect size (defined as the proportion of samples for which a given colocalization was significant) were calculated.

Reporting summary

Further information on research design is available in the Nature Portfolio Reporting Summary linked to this article.

Data availability

The single-cell RNA sequencing and spatial transcriptomics data generated in this study have been deposited in the Gene Expression Omnibus (GEO) database under accession code GSE281796 (https://www.ncbi.nlm.nih.gov/geo/query/acc.cgi?acc=GSE281796) The published spatial transcriptomics data that was used in this study are available in Datadryad (https://doi.org/10.5061/dryad.wpzgmsbv6) The published bulk RNA-seq data of GBM PDXs that was used in this study are available in the NCBI BioProject database under accession code: PRJNA548556 (https://www.ncbi.nlm.nih.gov/bioproject/PRJNA548556) The source data are provided in the Source Data file. Source data are provided with this paper.

Code availability

The code used to create the figures in this manuscript was uploaded to (https://github.com/rchanoch/GBM_Invasion_script).

References

1. Ostrom, Q. T. et al. CBTRUS statistical report: primary brain and other central nervous system tumors diagnosed in the United States in 2012–2016. *Neuro-Oncol*. **21**, v1–v100 (2019).
2. Horbinski, C., Berger, T., Packer, R. J. & Wen, P. Y. Clinical implications of the 2021 edition of the WHO classification of central nervous system tumours. *Nat. Rev. Neurol*. **18**, 515–529 (2022).
3. Wen, P. Y. et al. Glioblastoma in adults: a Society for Neuro-Oncology (SNO) and European Society of Neuro-Oncology (EANO) consensus review on current management and future directions. *Neuro-Oncol*. **22**, 1073–1113 (2020).
4. Stupp, R. et al. Radiotherapy plus concomitant and adjuvant temozolomide for glioblastoma. *N. Engl. J. Med*. **352**, 987–996 (2005).
5. Drumm, M. R. et al. Extensive brainstem infiltration, not mass effect, is a common feature of end-stage cerebral glioblastomas. *Neuro-Oncol*. **22**, 470–479 (2020).
6. Holland, E. C. Glioblastoma multiforme: The terminator. *Proc. Natl. Acad. Sci*. **97**, 6242–6244 (2000).
7. Brown, T. J. et al. Association of the extent of resection with survival in glioblastoma: a systematic review and meta-analysis. *JAMA Oncol*. **2**, 1460 (2016).

8. Jelsma, R. & Bucy, P. C. The treatment of glioblastoma multiforme of the brain. *J. Neurosurg.* **27**, 388–400 (1967).
9. Cuddapah, V. A., Robel, S., Watkins, S. & Sontheimer, H. A neurocentric perspective on glioma invasion. *Nat. Rev. Neurosci.* **15**, 455–465 (2014).
10. Huang-Hobbs, E. et al. Remote neuronal activity drives glioma progression through SEMA4F. *Nature* **619**, 844–850 (2023).
11. Peiffer, J. & Kleihues, P. Hans-Joachim Scherer (1906-1945), pioneer in glioma research. *Brain Pathol.* **9**, 241–245 (1999).
12. Miyai, M., Iwama, T., Hara, A. & Tomita, H. Exploring the vital link between glioma, neuron, and neural activity in the context of invasion. *Am. J. Pathol.* **193**, 669–679 (2023).
13. Scherer, H. J. Etude sur les gliomes. IV. Croissance des gliomes dans leurs rapports avec les substances blanches et grises du cerveau. *Bull. Assoc. Franç Etude du Cancer* **25**, 451–469 (1936).
14. Scherer, H. J. Sur le développement des structures dans les gliomes. *Deuxième Congrès. Int. de. Lutte Scientifique et. Soc. Contre le. Cancer* **2**, 250–254 (1937).
15. Patel, A. P. et al. Single-cell RNA-seq highlights intratumoral heterogeneity in primary glioblastoma. *Science* **344**, 1396–1401 (2014).
16. Neftel, C. et al. An integrative model of cellular states, plasticity, and genetics for glioblastoma. *Cell* **178**, 835–849.e21 (2019).
17. Couturier, C. P. et al. Single-cell RNA-seq reveals that glioblastoma recapitulates a normal neurodevelopmental hierarchy. *Nat. Commun.* **11**, 3406 (2020).
18. Chanoch-Myers, R., Wider, A., Suva, M. L. & Tirosh, I. Elucidating the diversity of malignant mesenchymal states in glioblastoma by integrative analysis. *Genome Med.* **14**, 106 (2022).
19. Hara, T. et al. Interactions between cancer cells and immune cells drive transitions to mesenchymal-like states in glioblastoma. *Cancer Cell* **39**, 779–792.e11 (2021).
20. Shibue, T. & Weinberg, R. A. EMT, CSCs, and drug resistance: the mechanistic link and clinical implications. *Nat. Rev. Clin. Oncol.* **14**, 611–629 (2017).
21. Puram, S. V. et al. Single-cell transcriptomic analysis of primary and metastatic tumor ecosystems in head and neck cancer. *Cell* **171**, 1611–1624.e24 (2017).
22. Jin, X. et al. Frizzled 4 regulates stemness and invasiveness of migrating glioma cells established by serial intracranial transplantation. *Cancer Res.* **71**, 3066–3075 (2011).
23. Yachi, K. et al. miR-23a promotes invasion of glioblastoma via HOXD10-regulated glial-mesenchymal transition. *Signal Transduct. Target. Ther.* **3**, 33 (2018).
24. Kim, Y. et al. Perspective of mesenchymal transformation in glioblastoma. *Acta Neuropathol. Commun.* **9**, 50 (2021).
25. Kahlert, U. D., Nikkhah, G. & Maciaczyk, J. Epithelial-to-mesenchymal(-like) transition as a relevant molecular event in malignant gliomas. *Cancer Lett.* **331**, 131–138 (2013).
26. Jin, X. et al. Targeting glioma stem cells through combined BMI1 and EZH2 inhibition. *Nat. Med.* **23**, 1352–1361 (2017).
27. Minata, M. et al. Phenotypic plasticity of invasive edge glioma stem-like cells in response to ionizing radiation. *Cell Rep.* **26**, 1893–1905.e7 (2019).
28. Greenwald, A. C. et al. Integrative spatial analysis reveals a multi-layered organization of glioblastoma. *Cell* **187**, 2485–2501.e26 (2024).
29. Venkataramani, V. et al. Glioblastoma hijacks neuronal mechanisms for brain invasion. *Cell* **185**, 2899–2917.e31 (2022).
30. Yu, K. et al. Surveying brain tumor heterogeneity by single-cell RNA sequencing of multi-sector biopsies. *Natl. Sci. Rev.* **7**, nwaa099 (2020).
31. Darmanis, S. et al. Single-Cell RNA-Seq Analysis of Infiltrating Neoplastic Cells at the Migrating Front of Human Glioblastoma. *Cell Rep.* **21**, 1399–1410 (2017).
32. Vaubel, R. A. et al. Genomic and phenotypic characterization of a broad panel of patient-derived xenografts reflects the diversity of glioblastoma. *Clin. Cancer Res.* **26**, 1094–1104 (2020).
33. Comba, A. et al. Spatiotemporal analysis of glioma heterogeneity reveals COL1A1 as an actionable target to disrupt tumor progression. *Nat. Commun.* **13**, 3606 (2022).
34. Heaton, H. et al. Souporcell: robust clustering of single-cell RNA-seq data by genotype without reference genotypes. *Nat. Methods* **17**, 615–620 (2020).
35. Neavin, D. et al. Demuxafy: improvement in droplet assignment by integrating multiple single-cell demultiplexing and doublet detection methods. *Genome Biol.* **25**, 94 (2024).
36. Kinker, G. S. et al. Pan-cancer single-cell RNA-seq identifies recurring programs of cellular heterogeneity. *Nat. Genet.* **52**, 1208–1218 (2020).
37. Mathewson, N. D. et al. Inhibitory CD161 receptor identified in glioma-infiltrating T cells by single-cell analysis. *Cell* **184**, 1281–1298.e26 (2021).
38. Civita, P., Valerio, O., Naccarato, A. G., Gumbleton, M. & Pilkington, G. J. Satellitosis, a crosstalk between neurons, vascular structures and neoplastic cells in brain tumours; early manifestation of invasive behaviour. *Cancers* **12**, 3720 (2020).
39. Tsai, H.-H. et al. Oligodendrocyte precursors migrate along vasculature in the developing nervous system. *Science* **351**, 379–384 (2016).
40. Wu, Y. et al. Neurodevelopmental hijacking of oligodendrocyte lineage programs drives glioblastoma infiltration. *Dev. Cell* **60**, 2420–2433 (2025).
41. Ratliff, M. et al. Individual glioblastoma cells harbor both proliferative and invasive capabilities during tumor progression. *Neuro-Oncol.* **25**, 2150–2162 (2023).
42. Manoharan, V. T. et al. Spatiotemporal modeling reveals high-resolution invasion states in glioblastoma. *Genome Biol.* **25**, 264 (2024).
43. Venkatesh, H. S. et al. Neuronal activity promotes glioma growth through neuroligin-3 secretion. *Cell* **161**, 803–816 (2015).
44. Brooks, L. J. et al. The white matter is a pro-differentiative niche for glioblastoma. *Nat. Commun.* **12**, 2184 (2021).
45. Kang, S. et al. Glioblastoma shift from bulk to infiltrative growth is guided by plexin-B2-mediated microglia alignment in invasive niches. *Nat. Cancer* **6**, 1505–1523 (2025).
46. Ubellacker, J. M. et al. Lymph protects metastasizing melanoma cells from ferroptosis. *Nature* **585**, 113–118 (2020).
47. Doroszko, M. et al. The invasion phenotypes of glioblastoma depend on plastic and reprogrammable cell states. *Nat. Commun.* **16**, 6662 (2025).
48. El-Botty, R. et al. Oxidative phosphorylation is a metabolic vulnerability of endocrine therapy and palbociclib resistant metastatic breast cancers. *Nat. Commun.* **14**, 4221 (2023).
49. LeBleu, V. S. et al. PGC-1α mediates mitochondrial biogenesis and oxidative phosphorylation in cancer cells to promote metastasis. *Nat. Cell Biol.* **16**, 992–1003 (2014).
50. Davis, R. T. et al. Transcriptional diversity and bioenergetic shift in human breast cancer metastasis revealed by single-cell RNA sequencing. *Nat. Cell Biol.* **22**, 310–320 (2020).
51. Cañellas-Socias, A. et al. Metastatic recurrence in colorectal cancer arises from residual EMP1+ cells. *Nature* **611**, 603–613 (2022).
52. Ridenour, D. A. et al. The neural crest cell cycle is related to phases of migration in the head. *Development* **141**, 1095–1103 (2014).
53. Vega, S. et al. Snail blocks the cell cycle and confers resistance to cell death. *Genes Dev.* **18**, 1131–1143 (2004).
54. Mazzoleni, S. et al. Epidermal Growth Factor Receptor Expression Identifies Functionally and Molecularly Distinct Tumor-Initiating Cells in Human Glioblastoma Multiforme and Is Required for Gliomagenesis. *Cancer Res.* **70**, 7500–7513 (2010).

55. Wakimoto, H. et al. Maintenance of primary tumor phenotype and genotype in glioblastoma stem cells. *Neuro-Oncol.* **14**, 132–144 (2011).
56. Hara, T. & Verma, I. M. Modeling gliomas using two recombinases. *Cancer Res.* **79**, 3983–3991 (2019).
57. Li, B. & Dewey, C. N. RSEM: accurate transcript quantification from RNA-Seq data with or without a reference genome. *BMC Bioinform* **12**, 323 (2011).
58. Tirosh, I. et al. Single-cell RNA-seq supports a developmental hierarchy in human oligodendroglioma. *Nature* **539**, 309–313 (2016).
59. Spitzer, A. et al. Deciphering the longitudinal trajectories of glioblastoma ecosystems by integrative single-cell genomics. *Nat. Genet.* **57**, 1168–1178 (2025).
60. Nomura, M. et al. The multilayered transcriptional architecture of glioblastoma ecosystems. *Nat. Genet.* **57**, 1155–1167 (2025).
61. Street, K. et al. Slingshot: cell lineage and pseudotime inference for single-cell transcriptomics. *BMC Genomics* **19**, 477 (2018).
62. Van den Berge, K. et al. Trajectory-based differential expression analysis for single-cell sequencing data. *Nat. Commun.* **11**, 1201 (2020).
63. Ravi, V. M. et al. Spatially resolved multi-omics deciphers bidirectional tumor-host interdependence in glioblastoma. *Cancer Cell* **40**, 639–655.e13 (2022).

Acknowledgements

This work was supported by Grant-in-Aid for JSPS Fellows from the Japan Society for the Promotion of Science (to T.H.), SENSHIN Medical Research Foundation (to T.H.), Kanae Foundation (to T.H.), Brain Research Foundation (to T.H.), American Brain Tumor Association (to T.H.), Seth M Boyer Foundation (to T.H.), N.I.H. R37CA245523 (to M.L.S.), N.I.H. R01CA258763 (to M.L.S.), Mark Foundation Emerging Leader Award (to M.L.S.), Sontag Foundation Distinguished Scientist Award (to M.L.S.), MGH Research Scholars (to M.L.S.), Broad Institute-Israel Science Foundation Collaborative Project Award (to I.T. and M.L.S.), European Research Council Consolidator Grant 101044318 (to I.T.), Zuckerman STEM Leadership Program (to I.T.), Mexican Friends New Generation (to I.T.),. I.T. is the incumbent of the Dr. Celia Zwillenberg-Fridman and Dr. Lutz Zwillenberg Career Development Chair. IMMediate Advanced Clinician Scientist-Program, Department of Medicine II, Medical Center–University of Freiburg and Faculty of Medicine, University of Freiburg, funded by the Bundesministerium für Bildung und Forschung (BMBF, Federal Ministry of Education and Research) – 01EO2103 (to R.H.).

Author contributions

R.C.M., T.H., A.C.G., M.L.S., and I.T. conceived the project, designed the study, interpreted results, and wrote the manuscript. R.C.M. and A.C.G. performed computational analyses. T.H. performed GBM model experiments. A.C.G. and E.C.F. performed spatial transcriptomics. R.H. performed antibody-based multiplexed imaging (CODEX) experiments. L.B. and H.R.W. helped generate plate-based scRNA-seq data. E.N.B., J.G., Z.B., A.J., J.M.H.F., W.A., and S.C.P. helped perform animal and pathological studies. C.B., J.B., R.G., and H.W. helped GBM model development.

Competing interests

I.T. is an advisory board member of Immunitas Therapeutics, and a scientific co-founder, equity holder and advisory board member of Cellyrix Therapeutics. M.L.S. is an equity holder, scientific co-founder, and advisory board member of Immunitas Therapeutics. The remaining authors declare no competing interests.

Additional information

Supplementary information The online version contains supplementary material available at https://doi.org/10.1038/s41467-026-70470-8.

Correspondence and requests for materials should be addressed to Toshiro Hara, Mario L. Suvà or Itay Tirosh.

Peer review information *Nature Communications* thanks anonymous reviewers for their contribution to the peer review of this work. A peer review file is available.

Reprints and permissions information is available at http://www.nature.com/reprints

---

[1]Department of Molecular Cell Biology, Weizmann Institute of Science, Rehovot, Israel. [2]Department of Cancer Biology, Dana-Farber Cancer Institute, Boston, MA, USA. [3]Broad Institute of Harvard and MIT, Cambridge, MA, USA. [4]Department of Pathology and Krantz-Family Center for Cancer Research, Massachusetts General Hospital and Harvard Medical School, Boston, MA, USA. [5]Department of Neurosurgery and Rogel Cancer Center, University of Michigan Medical School, Ann Arbor, MI, USA. [6]Biointerfaces Institute, University of Michigan, Ann Arbor, MI, USA. [7]Lunenfeld-Tanenbaum Research Institute, Mount Sinai Hospital, Toronto, ON, Canada. [8]Department of Molecular Genetics, University of Toronto, Toronto, ON, Canada. [9]Department of Medicine I, Medical Center – University of Freiburg, Faculty of Medicine, University of Freiburg, Freiburg, Germany. [10]Oncology Division, Tel Aviv Sourasky Medical Center, Tel Aviv, Israel. [11]Gray Faculty of Medical and Health Sciences, Tel Aviv University, Tel Aviv, Israel. [12]Neural Stem Cell Biology Unit, Division of Neuroscience, IRCCS San Raffaele Hospital, Via Olgettina, Milan, Italy. [13]Department of Pathology, University of Michigan Medical School, Ann Arbor, MI, USA. [14]The Leo M. Davidoff Department of Neurological Surgery, Albert Einstein College of Medicine, Montefiore Medical Center, Bronx, NY, USA. [15]Department of Neurosurgery, Massachusetts General Hospital and Harvard Medical School, Boston, MA, USA. [16]These authors contributed equally: Rony Chanoch-Myers, Toshiro Hara, and Alissa C. Greenwald. [17]These authors jointly supervised this work. Itay Tirosh, Mario L. Suvà, Toshiro Hara ✉e-mail: hara@umich.edu; Suva.Mario@mgh.harvard.edu; Itay.tirosh@weizmann.ac.il